Accepted Manuscript

Compressive strength of elderly vertebrae is reduced by disc degeneration and additional flexion

Ghislain Maquer[a], Jakob Schwiedrzik[a], Gerd Huber[b], Michael M. Morlock[b] and Philippe K. Zysset[a]

a Institute of Surgical Technology and Biomechanics, University of Bern, Stauffacherstrasse 78, 3014 Bern, Switzerland

b Institute of Biomechanics, Hamburg University of Technology, Denickestraße 15, 21073 Hamburg, Germany

Corresponding author:
Philippe K. Zysset
Institute of Surgical Technology and Biomechanics
University of Bern, Stauffacherstrasse 78, CH-3014 Bern, Switzerland
Tel.: +41 31 631 59 25; fax: +41 31 631 59 60
E-mail address: philippe.zysset@istb.unibe.ch

Grants:
Swiss National Science Foundation (SNF), grant n° 325230_147153
German Federal Ministry of Education and Research (BMBF), grant n° 01EC1005

Abstract: 227

Word count for the main text (Introduction to discussion): 4436

Number of tables: 2

Number of figures: 8 + 2 in appendix

Disclosure

None of the authors have conflict of interest regarding this manuscript.

Abstract

Computer tomography (CT)-based finite element (FE) models assess vertebral strength better than dual energy X-ray absorptiometry. Osteoporotic vertebrae are usually loaded via degenerated intervertebral discs (IVD) and potentially at higher risk under forward bending, but the influences of the IVD and loading conditions are generally overlooked. Accordingly, Magnetic Resonance Imaging was performed on 14 lumbar discs to generate FE models for the healthiest and most degenerated specimens. Compression, torsion, bending, flexion and extension conducted experimentally were used to calibrate both models. They were combined with CT-based FE models of 12 lumbar vertebral bodies to evaluate the effect of disc degeneration compared to a loading via endplates embedded in a stiff resin, the usual experimental paradigm. Compression and lifting were simulated, load and damage pattern were evaluated at failure. Adding flexion to the compression (lifting) and higher disc degeneration reduces the failure load (8-14%, 5-7%) and increases damage in the vertebrae. Under both loading scenarios, decreasing the disc height slightly increases the failure load; embedding and degenerated IVD provides respectively the highest and lowest failure load. Embedded vertebrae are more brittle, but failure loads induced via IVDs correlate highly with vertebral strength. In conclusion, osteoporotic vertebrae with degenerated IVDs are consistently weaker - especially under lifting, but clinical assessment of their strength is possible via FE analysis without extensive disc modelling, by extrapolating measures from the embedded situation.

Key words: finite element analysis, vertebral strength, osteoporosis, intervertebral disc degeneration, calibration

1. Introduction

With nearly half a million cases a year in Europe, osteoporotic vertebral fractures are a widespread condition with tremendous costs and morbidity (Johnell and Kanis 2005). Osteoporosis is characterized by bone loss and impaired bone morphology. Fracture occurs when the load on a bone is larger than its overload or fatigue strength. Strength and mineral density (BMD) are therefore highly related and non-invasive radiographic techniques were developed to evaluate the fracture risk. Yet, as Dual energy X-ray absorptiometry (DXA), the clinical surrogate for strength, accounts neither for morphology, nor for local variation of bone density (Griffith and Genant 2008) or loading conditions, it explains less than 70% of the strength variability (Lochmüller et al. 2002).

Quantitative computer tomography (QCT)-based finite element (FE) models of the vertebral body are used in clinical trials (Keaveny et al. 2007, Graeff et al. 2009, Chevalier et al. 2010, Graeff et al. 2013, Farahmand et al. 2013, Glüer et al. 2013, Kopperdahl et al. 2014) but not yet for diagnosis, although their strength predictions are more accurate than densitometric methods (Crawford et al. 2003, Dall'ara et al. 2012). To ensure uniform compression of the bone and overlook the degenerative states of elderly intervertebral discs (IVD) (Keller et al. 1993), the endplates are trimmed (vertebral sections) or embedded in a stiff resin (polymethylmethacrylate, PMMA). Both methods are reproducible, validated (Dall'ara et al. 2010, Chevalier et al. 2008) and highly correlated (Maquer et al. 2012) but common endplate failure cannot be replicated (Nekkanty et al. 2010, Maquer et al. 2014a). Compression overestimates the strength of osteoporotic vertebrae that are weaker under forward bending due to an altered trabecular structure (Homminga et al. 2004). The load distribution on the endplate is affected by alterations of the IVD due to degenerative processes (Adams and Roughley 2006). It seems relevant to account for the IVD in future FE analyses (Eswaran et al. 2007) but there is a lack of reliable degeneration-specific model (Lu et al. 2014). Most models are based on prior literature, with generic shapes and material properties (Fagan et al. 2002, Weisse et al. 2012, Park et al. 2013) without considering the inter-individual and experimental variability (Jones and Wilcox 2008).

Addressing these limitations, healthy and degenerated IVD models calibrated against in vitro tests and endplate embedding were used to load vertebral bodies under uniaxial compression

and lifting. The hypothesis of this study is that disc degeneration and forward flexion weaken osteoporotic vertebrae; its aim is to evaluate the influence of the loading conditions on the predicted vertebral failure load and damage distribution and to determine whether FE strength predictions would benefit from a better modelling of the IVD.

1.1. Specimen-specific modelling of the intervertebral disc

1.1.1. Preparation and selection of the specimens

Fourteen spinal units (T12-L1, L2-L3, L4-L5) were extracted from 6 human lumbar spines and frozen (-20°C) after approval of the Ethics Committee of the Medical University of Vienna. The specimens were thawed at room temperature (20°C) 24h before neural arch and most soft tissues, but IVDs were removed. The free caudal and cranial endplates were embedded in a 10 mm-thick layer PMMA (Fig. 1). MRI imaging was performed on the specimens placed in a water-filled container (0.9% saline) to avoid drying and ensure loading of the RF coil. T_1 weighted (T_R = 999 ms, T_E = 13 ms, 0.3 mm in-plane, 0.8 mm out-of-plane resolution) and quantitative T_2 images (T_R = 3650 ms, first echo: 12.5 ms, last echo: 275 ms, steps: 12.5 ms, 0.5 mm resolution) were acquired via a 3T system (Verio, Siemens Healthcare, Germany). The non-invasive evaluation of the specimens' degeneration was done independently by 2 experts based on their mid-sagittal appearance (Thompson et al. 1990), transverse T_2-maps (Watanabe et al. 2007) and Benneker score, validated against biochemical markers of degeneration (Benneker et al. 2005). The healthiest (Grade I) and most degenerated (Grade IV) spinal units were kept for testing. Please refer to Maquer et al. 2014b for more details.

1.1.2. MRI-based disc geometry

MRI data was also used mesh both specimens and determine their dimensions (Fig. 1). The discs were semi-automatically segmented from the T_{1w} images via ITKSnap (Yushkevich et al. 2006). Volume (V), cross-sectional area (CSA), average disc height (H) and size ratio (R) were determined (Eq. 1).

$$\mathrm{CSA} = \sum_{i}^{N} \mathrm{CSA_i} \qquad \mathrm{V} = \sum_{i}^{M} \mathrm{V_i} \qquad \mathrm{H} = \frac{\mathrm{V}}{\mathrm{CSA}} \qquad \mathrm{R} = \frac{\mathrm{H}}{\sqrt{\mathrm{CSA}}} \quad (1)$$

V was evaluated by summing the volume of the disc's voxels V_i (M voxels per disc) and CSA was computed by adding the CSA_i of the disc's voxels (N voxels per cross-section). A size ratio was obtained for the healthy (R_I) and degenerated IVDs (R_{IV}).

The segmented volumes were imported in Solidworks as .stl meshes via ScanTo3D (Dassault Systèmes, France) and 2 solids were generated by fitting surface patches onto the smoothened meshes. Partition between NP and AF (42% volume ratio, Goto et al. 2002, Moramarco et al. 2010, Wang et al. 2013) was performed on both solids that were meshed with quadratic tetrahedral elements in Cubit 12.2 (Sandia National Laboratory, USA). Element aspect ratio (Parthasarathy et al. 1994), condition number, scaled jacobian (Knupp et al. 2000), shape & size (Knupp et al. 2003), solution accuracy and CPU time required were evaluated and mesh and segmented volumes were compared.

1.1.3. Disc constitutive model

A time-independent constitutive law accounting for fibre dispersion around an average bundle direction was chosen (Gasser et al. 2006). It proved able to model annulus fibrosus (AF) (Malandrino et al. 2013) among other soft tissues (Pandolfi et al. 2008, Giordano et al.

2014). Neo-hookean material for the nucleus pulposus (NP) and AF's ground substance (Eq. 2) and Holzapfel-Gasser-Ogden (HGO) model for the annular fibres (Eq. 3) are available in Abaqus 6.13 (Dassault Systèmes, France).

$$\psi_{\mathrm{Iso}}(C_{10}, D) = C_{10}(J_1 - 3) + \frac{1}{D}\left\{\frac{(\det(F))^2 - 1}{2} - \ln(\det(F))\right\} \quad (2)$$

$$\psi_{\mathrm{Aniso}}(K_1, K_2, \kappa, \alpha) = \frac{K_1}{2K_2}\{\exp[K_2(\kappa J_1 + (1 - 3\kappa)J_f(\alpha) - 1)^2] - 1\} \quad (3)$$

With J_1 = trace(C*) and $J_f = a_0 C^* a_0$, first and pseudo-invariant of the unimodular right Cauchy-Green deformation tensor C* (det C*= 1). J_f is equal to the square of the stretch in the initial bundle direction $a_0 = [\cos(\alpha), \sin(\alpha), 0]^t$. The law features 8 constants (Fig. 2). The parameters of AF's matrix (C_{10}^{AF}, D^{AF}) and NP (C_{10}^{NP}, D^{NP}) are related to Young's modulus (E) and Poisson ratio (ν) via Eq. 4 (Holzapfel et al. 2006).

$$C_{10} = \frac{E}{4(1+\nu)} \text{ and } D = \frac{6(1-2\nu)}{E} \quad (4)$$

Two fibre families, active in tension (if J_f<1, ψ_{Aniso}=0), were placed in opposite directions and circumferentially by rotating the element's local coordinates system based on the AF's contours. The fibre parameters K_1, K_2, κ and α stand for fibre stiffness, rate of stiffness increase due to fibre recruitment, fibres dispersion and angle of the bundle (Li et al. 2013). Perfect fibre alignment along the average bundle direction is given by κ = 0 and an isotropic distribution by κ = 1/3. Those constants were equal for both families and homogenous in the AF.

1.1.4. Parameters identification against biomechanical tests

Five non-destructive quasi-static experiments were conducted successively (Fig. 3). Flexibility tests up to 8.5 Nm (Krismer et al. 2000) and compression up to 1300 N (Lin et al. 1978) were conducted without deterioration of the disc. The first loading consisted in 5 cycles of compression up to 1000 N were applied at 2000 N/min loading rate via a servo-hydraulic device (MTS, Bionix, USA). Then, 5 cycles of pure moments (-5 to 5 Nm) were conducted at 0.8°/s on both specimens in flexion, extension, axial torsion and lateral bending via a spine testing device (Gédet et al. 2007, 2009) to avoid artificial constraints (Panjabi 1988, Wilke et al. 1998a, Wilke et al. 1998b). A brushless DC motors (Maxon, Switzerland) applied the torque on the superior PMMA layer while the relative angular displacements of the vertebral bodies were computed from the positions of motion capture markers rigidly fixed to both layers (Optotrak 3020, Northern Digital, Canada, resolution 0.1 mm). Symmetrical behaviour was obtained in axial rotation ($R^2 = 0.96$, $p < 0.01$) and lateral bending ($R^2 = 0.97$, $p < 0.01$). More details are provided in (Maquer et al. 2014b and c).

After a sensitivity study performed on 4 mesh densities, the loadings were simulated on the IVD FE models (Abaqus 6.13). To mimic the experiments, compression (1000 N), torsion, bending, flexion (5 Nm), extension (-5 Nm) were applied to the superior nodes of each mesh whose caudal surfaces were constrained. To identify the model parameters, 5 markers (Fig. 3) corresponding to displacements (u) at regular load increments (every 200 N or 1 Nm) were selected on each experimental and simulated dataset to account for the non-linearity of the load-deflection response. The average loading-unloading curve of the 5^{th} experimental cycle was always chosen, the previous cycles serving as preconditioning. The difference between experiments and simulations was then minimized for all 5 tests at once using a Particle

Swarm Optimisation (PSO) (Clerc and Kennedy 2002). Eventually, the following problem was solved with parameters and variables bounds based on the literature (Eberlein et al. 2004, Gasser et al. 2006, Moramarco et al. 2010, Deb and Padhye 2010):

$$\arg\min_{P}\left(\sum_{i}^{5\ tests}\ \sum_{j}^{5\ markers}\left\{u_{i,j}^{sim}(P)-u_{i,j}^{exp}\right\}^{2}\right) \quad (5)$$

With:

$\mathrm{P}=\left[\mathrm{C}_{10}^{\mathrm{NP}},\mathrm{D}^{\mathrm{NP}},\mathrm{C}_{10}^{\mathrm{AF}},\mathrm{D}^{\mathrm{AF}},\mathrm{K}_1,\mathrm{K}_2,\kappa,\alpha\right]$

$\mathrm{C}_{10}^{\mathrm{NP}},\mathrm{C}_{10}^{\mathrm{AF}}\in\left[0\,;2\right]$ MPa; $\mathrm{D}^{\mathrm{NP}},\mathrm{D}^{\mathrm{AF}}\in\left[0\,;2\right]$ MPa^{-1}; $\mathrm{K}_1\in\left[0\,;1000\right]$ MPa;

$\mathrm{K}_2\in\left[0\,;2000\right]$; $\kappa\in\left[0;1/3\right]$; $\alpha\in\left[20;60\right]$ °.

Two sets of parameters (P_I and P_{IV}) were obtained for the healthy (Grade I) and degenerated IVDs (Grade IV). The optimisation's accuracy was evaluated by computing Concordance Correlation Coefficient (CCC, Lin 1989) and Root Mean Square Error (RMSE) between *in vitro* and *in silico* markers' deflection.

1.2. Specimen-specific modelling of the vertebral body

1.2.1. Scanning and testing of the vertebral bodies

In a previous study (Chevalier et al. 2008), 12 vertebral bodies from male donors freed from soft tissues and posterior elements had been scanned at 82 μm voxel size in a water-filled chamber (XtremeCT, 59.4 kV, 1000 mA, Scanco Medical AG, Zürich, Switzerland). After the scanning, the authors embedded the endplates of the vertebral bodies in 10-mm-thick PMMA layers. Each specimen was pre-conditioned with 10 cycles of tension-compression (200-400N) and compressed quasi-statically on a testing system (5560 Series

Table Model Systems, Instron, USA). The vertebral strength (F_{EXP}) was defined as the maximal load achieved at failure.

1.2.2. CT-based vertebral geometry

These high-resolution CT images were processed after noise removal filtering (Laplace–Hamming, Laib et al. 1998). The images were segmented between cortical and trabecular bone (masks), a volume was generated from the trabecular mask (Isosurf, Treece et al. 1999) and quadratic tetrahedral elements were fitted within the volume to mesh the trabecular bone. To represent the cortex, quadratic wedge elements were extruded from this trabecular mesh based on the thickness of the cortical mask (Fig. 4). The procedure was automatically performed using Medtool (www.dr-pahr.at) following Pahr and Zysset 2008.

1.2.3. Bone constitutive model

Bone volume fraction (BVTV) and trabecular fabric anisotropy, computed respectively from the local apparent BMD of the QCT image (Chevalier et al. 2008) and mean intercept length (Laib et al. 1998), were assigned automatically to each bony element via Medtool (Fig. 4). An orthotropic elasticity tensor was assigned to each element based on the obtained fabric (Zysset and Curnier 1995) and an anisotropic elastic-viscoplastic damage model (Schwiedrzik and Zysset 2013) was chosen to simulate the mechanical behaviour of bone. The elastic domain is bound by an anisotropic quadric criterion (Schwiedrzik et al. 2013) fitted to uni- and multi-axial strength tests (Rincon and Zysset 2009). The model features no rate dependence in elastic regime and includes hardening and softening calibrated against experimental data (Dall'Ara et al. 2010). Damage (D), a scalar reducing the elements' stiffness to mimic micro-cracks, was computed from accumulated plastic strain (stress-

softening). D varies between 0 (no damage) and 1 (total failure). The constitutive model was implemented in Fortran (UMAT). Mesh and material mapping sensitivity are available in Pahr and Zysset 2009.

1.3. Simulated scenarios

1.3.1. Boundary conditions and load cases

To simulate IVDs and endplate embedding, 2 discs were extruded from the endplates of the vertebrae meshes (Maquer et al. 2014a). The height of extrusion (H_I and H_{IV}) was calculated based on the size ratio of the discs being modelled (R_I or R_{IV}) and cross-sectional area of the extruded volume (CSA_{ext}):

$$H_{I/IV} = R_{I/IV}\sqrt{CSA_{ext}} \quad (6)$$

Again, a 42% volume ratio between NP and AF and quadratic tetrahedral elements were chosen for the meshing. The disc constitutive law was applied with the identified parameters to mimic healthy (P_IR_I) or degenerated ($P_{IV}R_{IV}$) IVDs. Embedding was simulated using linear elastic properties (E = 3000 MPa, ν = 0.3, Lewis 1997) and a fictitious healthy IVD with a degenerated thickness (P_IR_{IV}) was introduced.

Loading scenarios in clinical environment must be simple to be well-controlled. Uniaxial compression and combined flexion-compression (lifting) were conducted beyond yield on the vertebral bodies with each endplate condition (48 simulations). Under compression, an axial displacement was prescribed to the cranial surface of the superior disc: 1 mm for the embedding, 6 mm for the IVDs. To simulate lifting, angular and axial displacement were conducted proportionally so that both flexion and compression reached their yield point

simultaneously (Graeff et al. 2009). In that case, 0.06 rad for the embedding and 0.36 rad for the IVDs were applied around the posterior edge of the superior disc (Crawford and Keaveny 2004, Chevalier et al. 2008).

1.3.2. Failure load and damage evaluation

Axial reaction forces (N) and displacements (mm) were computed for each increment. The maximal load achieved during the simulation, failure load (F) (Fig. 4), was defined for each endplate condition: F_{PMMA}, $F_{P_IR_I}$, $F_{P_{IV}R_{IV}}$and $F_{P_IR_{IV}}$. They were compared to F_{EXP}, the experimental vertebral strength (Chevalier et al. 2008). Weighted mean damage (WMD) (Maquer et al. 2014a) was evaluated for 8 regions of interest (ROI) to estimate the damage accumulation at failure (Fig. 5):

$$\mathrm{WMD}_{ROI} = \frac{\sum(V_i * \mathrm{D_i})}{V_{ROI}} \quad (7)$$

V_{ROI} is the volume of the ROI, D_i and V_i are the damage level and volume of the i^{th} element of the ROI. Correlation coefficient (R^2) was computed for failure loads and paired two-tailed student's t-tests were performed for comparison with a significance level of 95%.

2. Results

2.1. Identification of the disc parameters

Table 1 displays the relevant information of the healthy (I) and degenerated (IV) specimens and the calibrated parameters. The degenerative status of the 14 IVDs is available in Maquer et al. 2014b. Height and CSA, evaluated from the MRI data, fitted the accepted range (Koeller et al. 1986, O'Connell et al. 2007). A larger size ratio was computed for the

healthy specimen ($R_I = 0.25$, $R_{IV} = 0.16$).

All MRI-based meshes presented good quality and similar deflections for all tests (< 5% difference in compression, flexion, extension, torsion and bending). As only a modest error (< 2%) was found between segmented and meshed volumes, the coarsest mesh density was chosen (IVD I: 1905 and IVD IV: 2843 elements) based on its CPU time (20 times shorter).

Each iteration of the parameter identification involved 5 simulations lasting few minutes each on 4 processors of a 3GHz PC with 24 GB RAM (1 GB used). Good fit quality was achieved against the experiments within 68 (I) and 92 (IV) iterations. RMSE in torsion was lower than 0.3°, did not exceed 0.5° in bending and 0.5 mm in compression. Correlations between *in silico* and *in vitro* markers' deflection were adequate for each individual test (CCC > 0.75) and high for all tests (CCC = 0.99).

Elastic modulus (E) and Poisson ratio (ν) were via Eq. 3. The healthy NP and AF matrix were both more compliant ($E_I^{NP} = 0.15$ MPa / $E_{IV}^{NP} = 0.98$ MPa, $E_I^{AF} = 1.16$ MPa / $E_{IV}^{AF} = 3.04$ MPa), but respectively less and more compressible than the degenerated ones ($\nu_I^{NP} = 0.48$ / $\nu_{IV}^{NP} = 0.42$, $\nu_I^{AF} = 0.34$ / $\nu_{IV}^{AF} = 0.38$). The AF matrix was consistently stiffer, but more compressible than the NP's regardless the degeneration grade. Yet, healthy AF fibres were much stiffer (K_1) with fibre recruitment coefficient (K_2) twice larger. The fibrillar organisation also differed, with better aligned fibres ($\kappa_I < \kappa_{IV}$) around a larger angle ($\alpha_I > \alpha_{IV}$) in the healthy IVD.

2.2. Evaluation of vertebral failure load

Under pure compression, significantly higher vertebral failure loads were computed with PMMA embedding ($F_{PMMA} = 3566 \pm 1358$ N, $p < 0.001$) compared to the IVDs and small but

significant differences were found between healthy ($F_{P_IR_I}$ = 2839 ± 1088 N) and degenerated IVD ($F_{P_{IV}R_{IV}}$= 2646 ± 973 N, $p < 0.001$). Reducing the height of the healthy IVD slightly but significantly increased the vertebral failure load ($F_{P_IR_{IV}}$= 2906 ± 1063 N, $p < 0.001$). The simulated failure loads were highly related to each other ($R^2 > 0.99$) and to F_{EXP} ($R^2 > 0.97$) (Table 2). Failure loads under lifting were significantly lower than under compression ($p < 0.001$). Furthermore, F_{PMMA} (3547 ± 1448 N), $F_{P_IR_{IV}}$ (2864 ± 1092 N), $F_{P_IR_I}$ (2689 ± 1075 N) and $F_{P_{IV}R_{IV}}$ (2470 ± 981 N) under lifting were significantly different from one another ($p < 0.001$) but highly correlated with the simulated (F_{PMMA}, $R^2 > 0.97$) and experimental (F_{EXP}, $R^2 > 0.96$) vertebral strength (Table 2). Under both loading scenarios, embedding and degenerated IVD provided respectively the highest and lowest failure load; decreasing the height of a healthy disc slightly increased the failure load ($F_{PMMA} > F_{P_IR_{IV}} > F_{P_IR_I} > F_{P_{IV}R_{IV}}$) (Fig. 6). Regression equations provided in Table 2 relate the failure loads with healthy and degenerated IVD under compression or lifting to the conventional embedded situation (F_{PMMA} and F_{EXP}).

2.3. Evaluation of the vertebral damage at failure

The vertebral body with embedded endplates did not achieve wedge failure, in contrast with a load induced via IVDs (Fig. 7). Conducting lifting with the IVDs led to significantly higher damage in the anterior regions of the cortical and trabecular bone than pure compression (Fig. 8). The damage level in all ROIs was systematically the lowest with embedded endplates (PMMA), regardless the loading and generally the highest with the degenerated IVDs ($P_{IV}R_{IV}$). The healthy IVDs (P_IR_I and P_IR_{IV}) usually provided intermediate values significantly different than $P_{IV}R_{IV}$ and PMMA with minor effect due to a height

reduction. The general tendency was $WMD_{PMMA} < WMD_{P_IR_{IV}} < WMD_{P_IR_I} < WMD_{P_{IV}R_{IV}}$.

3. Discussion

This work showed that adding flexion to compression (lifting) and higher disc degeneration reduces the failure load (8-14%, 5-7%) and increases damage in the vertebral body. Under both loading scenarios, decreasing the disc height slightly increases the failure load and embedding and degenerated IVD provides respectively the highest and lowest failure load. Embedding does not resemble a degenerated disc although failure loads induced via IVDs correlate highly with vertebral strength. Usual simplifications inherent to IVD modelling were limited thanks to MRI-based dimensions and calibration of the material properties against multiple experiments. Unlike µFE limited to small strains (Fields et al. 2010, Nekkanty et al. 2010, Yang et al. 2012), post-yield and damage behaviour of bone were examined via the latest image-based model (Schwiedrzik and Zysset 2013, Schwiedrzik et al. 2013).

Like the degenerative status, the IVD morphology can be accessed via MRI (Maquer et al. 2014b, Maquer et al. 2014c). This method yielded a thinner and larger degenerated IVD (Koeller et al. 1986, Wilke et al. 2006, Peloquin et al. 2014). Such data was accounted in the size ratio when extruding the discs from the vertebral body models.

IVD models are increasingly complex and often lack proper validation, which limits their clinical potential. A hyperelastic constitutive law (Gasser et al. 2006) was therefore chosen, without consideration for tissue heterogeneity other than anisotropy of the AF fibres and distinction nucleus/annulus or poroelasticity as the instantaneous response of the IVD is well replicated by such models (Jones and Wilcox 2008). Typically, the compressive loads are

essentially carried by the NP and AF matrix (Adams and Roughley 2006), while AF fibres withstand the bending and torsional loads (Haughton et al. 2000). Yet, radial expansion of the nucleus under compression (Poisson effect) generating hoop stresses in the annular fibres (Cortes and Elliott 2012). Hence, the calibration procedure was performed for 5 tests at once without other constraints than the parameter bounds. Still, this simple model was able to mimic the experimental response of the IVD (Fig.A1.). The calibrated parameters for NP and AF matrices were consistent with the increased compressibility and stiffness associated with the dehydration of the degenerated disc (Iatridis et al. 1997, Galbusera et al. 2014). The non-linear behaviour and organisation of the AF fibres was afflicted by degeneration (Inoue et al. 2011). The calibration occurring at the structural level, annular defects may have been homogenized, explaining the lower stiffness of the degenerated fibres (Adams and Roughley 2006). The smaller fibre angle for the degenerated IVD is coherent with its height loss. Finally, the degenerated fibres were widely distributed compared to the healthy situation, implying that a degenerated bundle requires extra tension for all its fibres to be aligned and active, affecting the fibres' reorientation (Guerin et al. 2006). The change of fibre angle along the circumference of the AF (Holzapfel et al. 2005) has been considered in early stages of this study, but did not improve the fit to the experiments.

Disc degeneration predisposes to failure of the anterior vertebral body (Adams et al. 2006). Yet, independently of processes involving the neural arch, this study confirmed that some degrees of flexion added to the compression put the osteoporotic vertebral body at higher risk of failure. The anterior damage was significantly higher and the deformations of the vertebral bodies loaded via IVDs indubitably reminded of wedge fractures. This disagrees with Yang et al. (2012) who found that the spatial distribution of stress within the vertebral body is not

significantly affected by a moderate flexion (5°). The failure load with IVDs was reached for ~ 6° of flexion, which concurs with *in vitro* wedge failure angles (4-6°, Adams et al. 2006, Lu et al. 2014). The IVD status also has immediate consequences on vertebral failure load and on damage accumulation but none is directly related to a height loss and must arise from the altered material properties. The highest damage level was observed in the sub-chondral trabecular bone. The bone being weaker under tensile and shear strains (Feng et al. 2000), large radial expansion of the nucleus under compression induces tension in the upper endplates, placing them at high risk of failure (Fields et al. 2010). Even if the lower pressurization in a degenerated disc should reduce the effect, its weaker and disorganised AF fibres are probably less able to constrain the radial expansion.

Experimental estimation of vertebral strength usually consists in the compression of vertebral bodies, whose endplates were embedded in stiff material. This technique prevents endplate deformations and transfers a portion of the load from the trabecular to the cortical bone (Eswaran et al. 2006) leading to a more brittle behaviour with concentrated damage and higher failure load reached after small deformations, which differs from the clinical situation (Fig.A.2) (Nekkanty et al. 2010, Maquer et al. 2014a). Yet, independently of the degenerative status of the IVDs, failure loads under compression or lifting are highly correlated with experimental and simulated vertebral strength ($R^2 > 0.97$). Accordingly, extensive modelling of the IVD could be avoided using regression equations determined against the conventional embedded situation. Failure occurs when a large region of the bone collapses. This region, essentially composed of the weakest trabecular elements (Stauber et al. 2014), is characteristic of each vertebral body, which explains the high correlations between failure loads achieved with different loading conditions (Maquer et al. 2014a).

Strengths of vertebral body models with embedded endplates were compared to failure loads of vertebral bodies loaded via two real IVDs (Lu et al. 2014). Moderate correlation was found ($R^2 = 0.68$), suggesting that loading via IVDs is not necessary to evaluate vertebral strength. Here, the opposite method was proposed: FE predictions with IVDs were compared to experimental vertebral strengths and higher correlation was achieved ($R^2 > 0.96$). The discrepancy can be explained by distinct experimental set-ups and distinct levels of disc degeneration. While embedding of isolated vertebrae ensures well-defined loading conditions (Buckley et al. 2007), the test of the spinal segments is not as controlled. Moreover, the degeneration grading of the IVDs does not necessarily reflects its mechanical properties (Maquer et al. 2014b).

Limitations can be mentioned. The specimens had been frozen and thawed before MRI and tests, but few freezing-unfreezing cycles do not affect the flexibility of spinal segments (Gleizes et al. 1998, Tan and Uppuganti 2012). The discs and vertebrae were from male donors to limit the effect of the gender, but the dissimilar disc heights and cross-sectional areas can also be induced by different body weights rather than degeneration (Nachemson et al. 1979). Statistical shape models may be useful to account for the inter-individual variability (Neubert et al. 2013, Peloquin et al. 2014). Modelling assumptions may explain the poorer fit of the compressive behaviour of the degenerated IVD. The healthy NP can be segmented (Swider et al. 2010, Reutlinger et al. 2014), but no sharp interface exists between degenerated NP and AF (Peng et al. 2006, Ellingson et al. 2013). Unable to segment the degenerated nucleus, the same dimensions were applied to both NPs (Goto et al. 2002, Moramarco et al. 2010 and Wang et al. 2013). Moreover, the fibres are distributed based on the AF's contour, which may be fine with a healthy disc, but degenerated bundles are often

disrupted due to the loss of NP pressurization (Adams and Roughley 2006) impacting their resistance to the radial expansion of the NP under compression (Michalek et al. 2010). To minimize the impact of those simplifications, NP and AF parameters were fitted independently and fibre dispersion κ was included in the model. Only two specific IVDs were used, but represented two extreme cases of degeneration. Finally, experimental strength (F_{EXP}, Chevalier et al. 2008) were consistently higher than the simulated values (F_{PMMA}) due to the non-viscous nature of the bone constitutive model. Fitting the viscosity term would provide a one-to-one correlation affecting equally all FE predictions.

In summary, osteoporotic vertebral bodies bonded to degenerated intervertebral discs can be up to 14% weaker, especially under lifting, but failure loads with IVDs correlate highly with vertebral strengths. Therefore, if damage propagation and failure mechanism are not required, the clinical assessment of failure load can be extrapolated from finite element simulations without extensive modelling of the discs, using regression equations determined against the conventional embedded situation. Furthermore, vertebral sections, providing equivalent strength predictions, can also be used to simplify the pre-processing and computing time (Maquer et al. 2012). This is clinically relevant, since FE prediction of bone strength can be used as an additional criterion to identify the individuals at risk (Kopperdahl et al. 2014).

Acknowledgments

Thanks to Michael L. Pretterklieber for providing the specimens (Center of Anatomy and Cell Biology, Department of Applied Anatomy, Medical University of Vienna, Austria), to Yan Chevalier for his HRpQCT images (Ludwig-Maximilian University of Munich, Germany) and to Dieter Pahr for the Medtool support (Vienna University of Technology, Austria). We also acknowledge Vaclav Brandejsky and Peter Vermathen (Department of Clinical Research, University of Berne, Switzerland) for the MRI data, Lorin M. Benneker (Department of Orthopaedic Surgery, Inselspital, University of Berne, Switzerland) and Atsuya Watanabe (Department of Orthopaedic Surgery, Teikyo University, Ichihara, Japan) for the intervertebral discs' grading as well as Alexander Bürki, Marc Laurent and Urs Röhrer for their support with the mechanical tests and MRI-compatible container (Institute of Surgical Technology and Biomechanics, University of Bern, Switzerland). The project was possible through funding from the Swiss National Science Foundation (SNF), grant n° 325230_147153 and the German Federal Ministry of Education and Research (BMBF) under Grant 01EC1005.

References

Adams, M.A., Pollintine, P., Tobias, J.H., Wakley, G.K., Dolan, P., 2006. Intervertebral disc degeneration can predispose to anterior vertebral fractures in the thoracolumbar spine. J. Bone Miner. Res. 21(9), 1409-1416, DOI: 10.1359/JBMR.060609.

Adams, M.A., Roughley, P.J., 2006. What is intervertebral disc degeneration, and what causes it? Spine 31(18), 2151–2161, DOI: 10.1097/01.brs.0000231761.73859.2c.

Benneker, L.M., Heini, P.F., Anderson, S.E., Alini, M., Ito, K., 2005. Correlation of radiographic and MRI parameters to morphological and biochemical assessment of intervertebral disc degeneration. Eur. Spine J. 14, 27–35, DOI: 10.1007/s00586-004-0759-4.

Bergmann, G. 2008. Charité Universitaetsmedizin Berlin "OrthoLoad". Retrieved Oct. 15, 2014 from http://www.OrthoLoad.com

Buckley, J.M., Loo, K., Motherway, J., 2007. Comparison of quantitative computed tomography-based measures in predicting vertebral compressive strength. Bone 40(3), 767-774, DOI: 10.1016/j.bone.2006.10.025.c.

Chevalier, Y., Charlebois, M., Pahr, D., Varga, P., Heini, P., Schneider, E., Zysset, P., 2008. A patient-specific finite element methodology to predict damage accumulation in vertebral bodies under axial compression, sagittal flexion and combined loads. Comput. Methods Biomech. Biomed. Eng. 11, 477–487, DOI: 10.1080/10255840802078022.

Chevalier, Y., Quek, E., Borah, B., Gross, G., Stewart, J., Lang, T., Zysset, P., 2010. Biomechanical effects of teriparatide in women with osteoporosis treated previously with alendronate and risedronate: results from quantitative computed tomography-based finite element analysis of the vertebral body. Bone 46(1), 41-48, doi:10.1016/j.bone.2009.09.032.

Clerc, M., Kennedy, J., 2002. The particle swarm-explosion, stability, and convergence in a

multidimensional complex space. IEEE Trans. Evol. Comput. 6(1), 58-73, DOI: 10.1109/4235.985692.

Cortes, D. H., Elliott, D. M., 2012. Extra-fibrillar matrix mechanics of annulus fibrosus in tension and compression. Biomech. Model. Mechan. 11(6), 781-790, DOI: 10.1007/s10237-010-0194-x.

Crawford, R.P., Cann, C.E., Keaveny, T.M., 2003. Finite element models predict in vitro vertebral body compressive strength better than quantitative computed tomography. Bone 33(4), 744–750, DOI: 10.1115/1.1589772.

Crawford, R.P., Keaveny, T.M., 2004. Relationship between axial and bending behaviors of the human thoracolumbar vertebra. Spine 29(20), 2248-2255, DOI: 10.1097/01.brs.0000142435.90314.3b.

Dall'Ara, E., Schmidt, R., Pahr, D., Varga, P., Chevalier, Y., Patsch, J., Kainberger, F., Zysset, P., 2010. A nonlinear finite element model validation study based on a novel experimental technique for inducing anterior wedge-shape fractures in human vertebral bodies in vitro. J. Biomech. 43, 2374–2380, DOI: 10.1016/j.jbiomech.2010.04.023.

Dall'Ara, E., Pahr, D., Varga, P., Kainberger, F., Zysset P. 2012. QCT-based finite element models predict human vertebral strength in vitro significantly better than simulated DEXA. Osteoporosis Int. 23(2), 563-72, DOI: 10.1007/s00198-011-1568-3.

Deb, K., and Padhye, N., 2010. Development of efficient particle swarm optimizers by using concepts from evolutionary algorithms. In Proceedings of the 12th annual conference on Genetic and evolutionary computation, 55-62, DOI: 10.1145/1830483.1830492.

Eberlein, R., Holzapfel, G.A., Fröhlich, M., 2004. Multi-segment FEA of the human lumbar spine including the heterogeneity of the annulus fibrosus. Comput. Mech. 34(2), 147-163, DOI: 10.1007/s00466-004-0563-3.

Ellingson, A.M., Mehta, H., Polly, D.W., Ellermann, J., Nuckley, D.J., 2013. Disc

degeneration assessed by quantitative T2* correlated with functional lumbar mechanics. Spine 38(24), E1533–E1540, DOI: 10.1097/BRS.0b013e3182a59453.

Eswaran, S.K., Gupta, A., Adams, M.F., Keaveny, T.M., 2006. Cortical and trabecular load sharing in the human vertebral body. J. Bone Miner. Res. 21(2), 307– 314, DOI: 10.1359/JBMR.051027.

Eswaran, S.K., Gupta, A., Keaveny, T.M., 2007. Locations of bone tissue at high risk of initial failure during compressive loading of the human vertebral body. Bone 41, 733–739, DOI: 10.1016/j.bone.2007.05.017.

Fagan, M.J., Julian, S., Siddall, D.J., Mohsen, A.M., 2002. Patient-specific spine models. Part 1: finite element analysis of the lumbar intervertebral disc-a material sensitivity study. Proc. Inst. Mech. Eng. [H] 216(5), 299–314, DOI: 10.1243/09544110260216577.

Farahmand, P., Marin, F., Hawkins, F., Möricke, R., Ringe, J.D., Glüer, C.C., Papaioannou, N., Minisola, S., Martínez, G., Nolla, J.M., Niedhart, C., Guañabens, N., Nuti, R., Martín-Mola, E., Thomasius, F., Peña, J., Graeff, C., Kapetanos, G., Petto, H., Gentzel, A., Reisinger, A., Zysset, P.K., 2013. Early changes in biochemical markers of bone formation during teriparatide therapy correlate with improvements in vertebral strength in men with glucocorticoid-induced osteoporosis. Osteoporosis Int. 24(12), 2971-2981, DOI: 10.1007/s00198-013-2379-5.

Feng, Z., Rho, J., Han, S., Ziv, I., 2000. Orientation and loading condition dependence of fracture toughness in cortical bone. Mater. Sci. Eng. C 11(1), 41-46, DOI: 10.1016/S0928-4931(00)00142-9.

Fields, A.J., Lee, G.L., Keaveny, T.M., 2010. Mechanisms of initial endplate failure in the human vertebral body. J. Biomech. 43(16), 3126-3131, DOI: 10.1016/j.jbiomech.2010.08.002.

Galbusera, F., van Rijsbergen, M., Ito, K., Huyghe, J.M., Brayda-Bruno, M., Wilke, H.J., 2014. Ageing and degenerative changes of the intervertebral disc and their impact on spinal flexibility. Eur. Spine J., 1-9, DOI: 10.1007/s00586-014-3203-4.

Gasser, T.C., Ogden, R.W., Holzapfel, G.A., 2006. Hyperelastic modelling of arterial layers with distributed collagen fibre orientations. J. R. Soc. Interface 3(6), 15-35, DOI: 10.1098/rsif.2005.0073.

Gédet P., Thistlethwaite, P.A., Ferguson, S.J., 2007. Minimizing errors during in vitro testing of multisegmental spine specimens: considerations for component selection and kinematic measurement, J. Biomech. 40, 1881-1885, DOI: 10.1016/j.jbiomech.2006.07.024.

Gédet, P., Thistlethwaite, P.A., Ferguson, S.J., 2009. Comparative biomechanical investigation of a modular dynamic lumbar stabilization system and the dynesys system, Eur. Spine J. 18, 1504-1511, DOI: 10.1007/s00586-009-1077-7.

Giordano, C., Cloots, R.J.H., van Dommelen, J.A.W., Kleiven, S., 2014. The influence of anisotropy on brain injury prediction. J. Biomech, DOI: 10.1016/j.jbiomech.2013.12.036.

Gleizes, V., Viguier, E., Feron, J.M., Canivet, S., Lavaste, F, 1998. Effects of freezing on the biomechanics of the intervertebral disc. Surg. Radiol. Anat. 20, 403-7, DOI: 10.1007/BF01653130.

Glüer, C.C., Marin, F., Ringe, J.G., Hawkins, F., Möricke, R., Papaioannu, N., Farahmand, P., Minisola, S., Martínez, G., Nolla, J.M., Niedhart, C., Guanabens, N., Nuti, R., Martín-Mola, E., Thomasius, F., Kapetanos, G., Peña, J., Graeff, C., Petto, H., Sanz, B., Reisinger, A., Zysset, P.K., 2013. Comparative effects of teriparatide and risedronate in glucocorticoid-induced osteoporosis in men: 18-month results of the EuroGIOPs trial. J. Bone Miner. Res. 28(6), 1355-1368, DOI: 10.1002/jbmr.1870.

Goto, K., Tajima, N., Chosa, E., Totoribe, K., Kuroki, H., Arizumi, Y., Arai, T., 2002. Mechanical analysis of the lumbar vertebrae in a three-dimensional finite element method model in which intradiscal pressure in the nucleus pulposus was used to establish the model. J. Orthop. Sci. 7(2), 243-246, DOI: 10.1007/s007760200040.

Graeff, C., Chevalier, Y., Charlebois, M., Varga, P., Pahr, D., Nickelsen, T.N., Morlock,

M.M., Glüer, C.C., Zysset, P.K., 2009. Improvements in vertebral body strength under teriparatide treatment assessed in vivo by finite element analysis: results from the EUROFORS study. J. Bone Miner. Res. 24(10), 1672-80, DOI: 10.1359/JBMR.090416.

Graeff, C., Marin, F., Petto, H., Kayser, O., Reisinger, A., Peña, J., Zysset, P.K., Glüer, C.C., 2013. High resolution quantitative computed tomography-based assessment of trabecular microstructure and strength estimates by finite-element analysis of the spine, but not DXA, reflects vertebral fracture status in men with glucocorticoid-induced osteoporosis. Bone 52(2), 568-577, DOI: 10.1016/j.bone.2012.10.036.

Griffith, J.F., Genant, H.K. 2008. Bone mass and architecture determination: state of the art. Best Pract. Res. Clin. Endocrinol. Metab. 22, 737–764, DOI: 10.1016/j.beem.2008.07.003.

Guerin, H.A.L., Elliott, D.M., 2006. Degeneration affects the fiber reorientation of human annulus fibrosus under tensile load. J. Biomech. 39(8), 1410-1418, DOI: 10.1016/j.jbiomech.2005.04.007.

Haughton, V.M., Schmidt, T.A., Keele, K., An, H.S., Lim, T.H., 2000. Flexibility of lumbar spinal motion segments correlated to type of tears in the annulus fibrosus. J. Neurosurg. 92, 81–6, URL: http://thejns.org/doi/abs/10.3171/spi.2000.92.1.0081.

Holzapfel, G.A., Ogden, R.W., 2006. Mechanics of biological tissue Vol. 10, 3-540, Springer, Berlin.

Holzapfel, G. A., Schulze-Bauer, C. A. J., Feigl, G., & Regitnig, P. 2005. Single lamellar mechanics of the human lumbar anulus fibrosus. Biomechanics and modeling in mechanobiology, 3(3), 125-140. DOI: 10.1007/s10237-004-0053-8.

Homminga, J., Van-Rietbergen, B., Lochmüller, E.M., Weinans, H., Eckstein, F., Huiskes, R., 2004. The osteoporotic vertebral structure is well adapted to the loads of daily life, but not to infrequent error loads. Bone 343, 510–516, DOI: 10.1016/j.bone.2003.12.001.

Iatridis, J.C., Setton, L.A., Weidenbaum, M., Mow, V.C., 1997. Alterations in the mechanical behavior of the human lumbar nucleus pulposus with degeneration and aging. J. Orthop. Res. 15(2), 318-322, DOI: 10.1002/jor.1100150224.

Inoue, N., Espinoza Orías, A.A., 2011. Biomechanics of intervertebral disk degeneration. Orthop. Clin. N. Am.42(4), 487-499, DOI: 10.1016/j.ocl.2011.07.001.

Johnell, O., Kanis, J., 2005. Epidemiology of osteoporotic fractures. Osteoporos Int. 16(Suppl 2), S3–S7, DOI: 10.1359/JBMR.050304.

Jones, A.C., Wilcox, R.K., 2008. Finite element analysis of the spine: towards a framework of verification, validation and sensitivity analysis. Med. Eng. Phys. 30(10), 1287-1304, DOI: 10.1016/j.medengphy.2008.09.006.

Keaveny, T.M., Donley, D.W., Hoffmann, P.F., Mitlak, B.H., Glass, E.V., Martin J.A.S., 2007. Effects of teriparatide and alendronate on vertebral strength as assessed by finite element modelling of qct scans in women with osteoporosis. J. Bone. Miner. Res. 221, 149–157, DOI: 10.1359/JBMR.061011.

Keller, T.S., Ziv, I., Moeljanto, E., Spengler, D.M., 1993. Interdependence of lumbar disc and subdiscal bone properties: a report of the normal and degenerated spine. J. Spinal Disord. 6, 106–113.

Knupp, P.M., 2000. Achieving finite element mesh quality via optimization of the Jacobian matrix norm and associated quantities. Part 1—a framework for surface mesh optimization. Int. J. Numer. Meth. Eng. 48(3), 401-420, DOI: 10.1002/(SICI)1097-0207(20000530)48:3<401::AID-NME880>3.0.CO;2-D.

Knupp, P.M., 2003. Algebraic mesh quality metrics for unstructured initial meshes. Finite Elem. Anal. Des. 39(3), 217-241, DOI: 10.1016/S0168-874X(02)00070-7.

Koeller, W., Muehlhaus, S., Meier, W., Hartmann, F., 1986. Biomechanical properties of human intervertebral discs subjected to axial dynamic compression—influence of age and degeneration. J. Biomech. 19(10), 807-816, DOI: 10.1016/0021-9290(86)90131-

4.

Kopperdahl, D.L., Aspelund, T., Hoffmann, P.F., Sigurdsson, S., Siggeirsdottir, K., Harris, T.B., Gudnason, V., Keaveny, T.M., 2014. Assessment of incident spine and hip fractures in women and men using finite element analysis of CT scans. J. Bone Miner. Res. 29(3), 570–580, DOI: 10.1002/jbmr.2069.

Krismer, M., Haid, C., Behensky, H., Kapfinger, P., Landauer, F., Rachbauer, F., 2000. Motion in lumbar functional spine units during side bending and axial rotation moments depending on the degree of degeneration. Spine 25(16), 2020-2027, DOI: 10.1097/00007632-200008150-00004.

Laib, A., Huselmann, H.J., Regsegger, P., 1998. In vivo high-resolution 3D-QCT of the human forearm. Technol Health Care. 6(5-6), 329–337, URL: http://e-collection.library.ethz.ch/eserv/eth:22792/eth-22792-02.pdf.

Lewis, G., 1997. Properties of acrylic bone cement: State of the art review. J. Biomed. Mater Res. 38(2), 155 –182, DOI: 10.1002/(SICI)1097-4636(199722)38:2<155::AID-JBM10>3.0.CO;2-C.

Li, W.G., Going, J., Hill, N.A., & Luo, X.Y., 2013. Breaking analysis of artificial elastic tubes and human artery. Int. J. Appl. Mech. 5(03), DOI: 10.1142/S1758825113500245.

Lin, H.S., Liu, Y.K., Adams, K.H., 1978. Mechanical response of the lumbar intervertebral joint under physiological (complex) loading. J. Bone Joint Surg. 60(1), 41-55, URL: http://jbjs.org/article.aspx?articleid=17371.

Lin, L.K, 1989. A concordance correlation coefficient to evaluate reproducibility. Biometrics 45(1), 255-268, DOI: 10.2307/2532051.

Lochmüller, E.M., Bürklein, D., Kuhn, V., Glaser, C., Müller, R., Glüer, C.C., Eckstein, F., 2002. Mechanical strength of the thoracolumbar spine in the elderly: prediction from in situ dual-energy X-ray absorptiometry, quantitative computed tomography (QCT),

upper and lower limb peripheral QCT, and quantitative ultrasound. Bone 31(1), 77-84, DOI: 10.1016/S8756-3282(02)00792-5.

Lu, Y., Maquer, G., Museyko, O., Püschel, K., Engelke, K., Zysset, P., Morlock M., Huber G., 2014. Finite element analyses of human vertebral bodies embedded in polymethylmethalcrylate or loaded via the hyperelastic intervertebral disc models provide equivalent predictions of experimental strength. J. Biomech., DOI: 10.1016/j.jbiomech.2014.04.015

Malandrino, A., Noailly, J., Lacroix, D., 2013. Regional annulus fibre orientations used as a tool for the calibration of lumbar intervertebral disc finite element models. Comput. Methods Biomech. Biomed. Engin. 16(9), 923-928, DOI: 10.1080/10255842.2011.644539.

Maquer, G., Dall'Ara, E., Zysset, P.K., 2012. Removal of the cortical endplates has little effect on ultimate load and damage distribution in QCT-based voxel models of human lumbar vertebrae under axial compression. J. Biomech. 45, 1733–1738, DOI: 10.1016/j.jbiomech.2012.03.019.

Maquer, G., Schwiedrzik, J. and Zysset, P.K., 2014a. Embedding of human vertebral bodies leads to higher ultimate load and altered damage localisation under axial compression. Comput. Methods Biomech. Biomed. Eng. 17(12), 1311-1322, DOI: 10.1080/10255842.2012.744400.

Maquer, G., Brandejsky, V., Benneker, L. M., Watanabe, A., Vermathen, P., Zysset, P. K., 2014b. Human intervertebral disc stiffness correlates better with the Otsu threshold computed from axial T2 map of its posterior annulus fibrosus than with clinical classifications. Med. Eng. Phys. 36(2), 219–225, DOI: 10.1016/j.medengphy.2013.11.008.

Maquer, G., Laurent, M., Brandejsky, V., Pretterklieber, M.L., Zysset P.K., 2014c. Finite element-based non-linear normalization of human lumbar intervertebral disc stiffness to account for its morphology. J. Biomech. Eng. 136(6), DOI: 10.1115/1.4027300.

Michalek, A. J., Funabashi, K. L., & Iatridis, J. C. 2010. Needle puncture injury of the rat intervertebral disc affects torsional and compressive biomechanics differently. European Spine Journal, 19(12), 2110-2116, DOI: 10.1007/s00586-010-1473-z

Moramarco, V., Perez del Palomar, A., Pappalettere, C., & Doblaré, M., 2010. An accurate validation of a computational model of a human lumbosacral segment. J. Biomech. 43(2), 334-342, DOI: 10.1016/j.jbiomech.2009.07.042.

Nachemson, A.L., Schultz, A.B., Berkson, M.H., 1979. Mechanical properties of human lumbar spine motion segments: influences of age, sex, disc level and degeneration. Spine 4, 1–8, DOI: 10.1097/00007632-197901000-00001.

Nekkanty, S., Yerramshetty, J., Kim, D., Zauel, R., Johnson, E., Cody, D.D., Yeni, Y.N., 2010. Stiffness of the endplate boundary layer and endplate surface topography are associated with brittleness of human whole vertebral bodies. Bone 47, 783–789, DOI: 10.1016/j.bone.2010.07.001.

O'Connell, G.D., Vresilovic, E.J., Elliott, D.M., 2007. Comparison of animals used in disc research to human lumbar disc geometry. Spine 32(3), 328-333, DOI: 10.1097/01.brs.0000253961.40910.c1.

Pahr, D.H., Zysset, P.K., 2008. From high-resolution CT data to finite element models: development of an integrated modular framework. Comput. Methods Biomech. Biomed. Eng. 12, 45-57, DOI: 10.1080/10255840802144105.

Pahr, D.H., Zysset, P.K., 2009. A comparison of enhanced continuum FE with micro FE models of human vertebral bodies. J. Biomech. 424, 455-462, DOI: 10.1016/j.jbiomech.2008.11.028.

Pandolfi, A., Holzapfel, G.A., 2008. Three-dimensional modeling and computational analysis of the human cornea considering distributed collagen fibril orientations. J. Biomech. Eng. 130(6), DOI: 10.1115/1.2982251.

Panjabi, M.M., 1988. Biomechanical evaluation of spinal fixation devices: a conceptual

framework. Spine 13(10), 1129–1134, DOI: 10.1097/00007632-198810000-00013.

Park, W.M., Kim, K., Kim, Y.H., 2013. Effects of degenerated intervertebral discs on intersegmental rotations, intradiscal pressures, and facet joint forces of the whole lumbar spine. Comput. Biol. Med. 43(9), 1234-1240, DOI: 10.1016/j.compbiomed.2013.06.011.

Parthasarathy, V.N., Graichen, C.M., Hathaway, A.F., 1994. A comparison of tetrahedron quality measures. Finite Elem. Anal. Des. 15(3), 255-261, DOI: 10.1016/0168-874X(94)90033-7.

Peloquin, J.M., Yoder, J.H., Jacobs, N.T., Moon, S.M., Wright, A.C., Vresilovic, E.J., Elliott, D.M., 2014. Human L3L4 intervertebral disc mean 3D shape, modes of variation, and their relationship to degeneration. J.Biomech, DOI: 10.1016/j.jbiomech.2014.04.014.

Peng, B., Wu, W., Hou, S., Li, P., Zhang, C., and Yang, Y., 2006. The pathogenesis and clinical significance of a high-intensity zone (hiz) of lumbar intervertebral disc on mr imaging in the patient with discogenic low back pain. Eur. Spine J. 15(5), 583–587, DOI: 10.1007/s00586-005-0892-8.

Reutlinger, C., Bürki, A., Brandejsky, V., Ebert, L., Büchler, P., 2014. Specimen specific parameter identification of ovine lumbar intervertebral discs: On the influence of fibre–matrix and fibre–fibre shear interactions. J. Mech. Behav. Biomed., 30, 279-289, DOI: 10.1016/j.jmbbm.2013.11.019.

Ribeiro, N., Fernandes, P. C., Lopes, D. S., Folgado, J., Fernandes, P., 2009. 3-D solid and finite element modeling of biomechanical structures-a software pipeline. In 7th EUROMECH Solid Mechanics Conference, Lisbon, Portugal, URL: https://fenix.tecnico.ulisboa.pt/downloadFile/2589867692870/paper.pdf.

Rincon-Kohli L., Zysset P., 2009. Multi-axial mechanical properties of human trabecular bone. J. Biomech. Model. Mechanobiol. 8(3), 195–208, DOI: 10.1007/s10237-008-0128-z.

Schwiedrzik, J.J., Zysset, P.K., 2013. An anisotropic elastic-viscoplastic damage model for bone tissue. Biomech. Model. Mechan. 12(2), 201-213, DOI: 10.1007/s10237-012-0392-9.

Schwiedrzik, J.J., Wolfram, U., Zysset, P.K., 2013. A generalized anisotropic quadric yield criterion and its application to bone tissue at multiple length scales. Biomech. Model. Mechan. 12(6), 1155-1168, DOI: 10.1007/s10237-013-0472-5.

Stauber, M., Nazarian, A., Müller, R., 2014. Limitations of global morphometry in predicting trabecular bone failure. J. Bone Miner. Res. 29(1), 134-141, DOI: 10.1002/jbmr.2006.

Swider, P., Pedrono, A., Ambard, D., Accadbled, F., Sales de Gauzy, J., 2010. Substructuring and poroelastic modelling of the intervertebral disc. J. Biomech. 43(7), 1287-1291, DOI: 10.1016/j.jbiomech.2010.01.006.

Tan, J.S., Uppuganti, S., 2012. Cumulative multiple freeze-thaw cycles and testing does not affect subsequent within-day variation in intervertebral flexibility of human cadaveric lumbosacral spine. Spine 37, E1238–42, DOI: 10.1097/BRS.0b013e31826111a3.

Thompson, J.P., Pearce, R.H,, Schechter, M.T., Adams, M.E., Tsang, I.K., Bishop, P.B., 1990. Preliminary evaluation of a scheme for grading the gross morphology of the human intervertebral disc. Spine 15, 411–5, URL: http://www.orthochina.com/uploadimage/20090529140246.pdf.

Treece, G.M., Prager, R.W., Gee, A.H., 1999. Regularised marching tetrahedra: improved iso-surface extraction. Comput. Graph. 23(4), 583-598, DOI: 10.1016/S0097-8493(99)00076-X.

Wang, S., Park, W.M., Kim, Y.H., Cha, T., Wood, K., Li, G., 2013. *In vivo* loads in the lumbar L3–4 disc during a weight lifting extension. Clin. Biomech., DOI: 10.1016/j.clinbiomech.2013.11.018.

Watanabe, A., Benneker, L.M., Boesch, C., Watanabe, T., Obata, T., Anderson, S.E., 2007. Classification of intervertebral disk degeneration with axial T2 mapping. A.J.R. 189,

936–42, DOI: 10.2214/AJR.07.2142.

Weisse, B., Aiyangar, A.K., Affolter, C., Gander, R., Terrasi, G.P., Ploeg, H., 2012. Determination of the translational and rotational stiffnesses of an L4–L5 functional spinal unit using a specimen-specific finite element model. J. Mech. Behav. Biomed. 13, 45-61, DOI: 10.1016/j.jmbbm.2012.04.002.

Wilke, H.J., Wenger, K., Claes, L., 1998a. Testing criteria for spinal implants: recommendations for the standardization of in vitro stability testing of spinal implants. Eur. Spine J. 7, 148–154, DOI: 10.1007/s005860050045.

Wilke, H.J., Jungkunz, B., Wenger, K., Claes, L.E., 1998b. Spinal segment range of motion as a function of in vitro test conditions: effects of exposure period, accumulated cycles, angular deformation rate, and moisture condition. Anat. Rec. 251(1), 15-19, DOI: 10.1002/(SICI)1097-0185(199805)251:1<15::AID-AR4>3.0.CO;2-D.

Wilke, H.J., Rohlmann, F., Neidlinger-Wilke, C., Werner, K., Claes, L., Kettler, A., 2006. Validity and interobserver agreement of a new radiographic grading system for intervertebral disc degeneration: Part I. Lumbar spine. Eur. Spine J. 15(6), 720-730, DOI: 10.1007/s00586-005-1029-9.

Yang, H., Nawathe, S., Fields, A.J., Keaveny, T.M., 2012. Micromechanics of the human vertebral body for forward flexion. J. Biomech. 45(12), 2142-2148, DOI: 10.1016/j.jbiomech.2012.05.044.

Yushkevich, P.A., Piven, J., Hazlett, H.C., Smith, R.G., Ho, S., Gee, J.C., Gerig G., 2006. User-guided 3d active contour segmentation of anatomical structures: significantly improved efficiency and reliability. NeuroImage 31, 1116 – 1128, DOI: 10.1016/j.neuroimage.2006.01.015.

Zysset, P.K., Curnier, A., 1995. An alternative model for anisotropic elasticity based on fabric tensors. Mech Mater. 21(4), 243-250, DOI: 10.1016/0167-6636(95)00018-6.

Figures

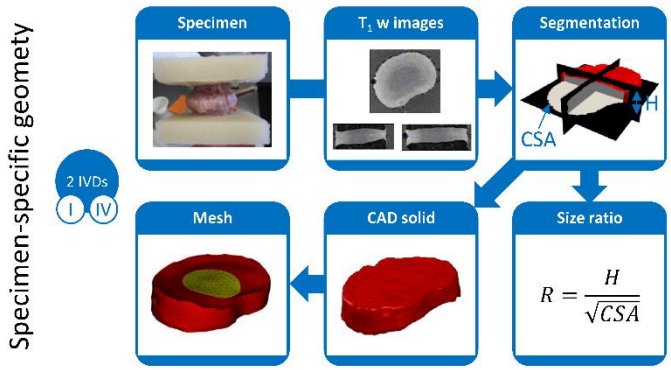

Fig.1. MRI-based FE meshes were generated from T_1 weighted images of the healthy (grade I) and degenerated (grade IV) specimens. Both discs were segmented. Size ratio (R) was computed for each specimen from height (H) and cross-sectional area (CSA) established from the segmented volume. Central nucleus (yellow) and the surrounding annulus (red) were partitioned and the volumes meshed. The meshing pipeline was adapted from Ribeiro et al. 2009.

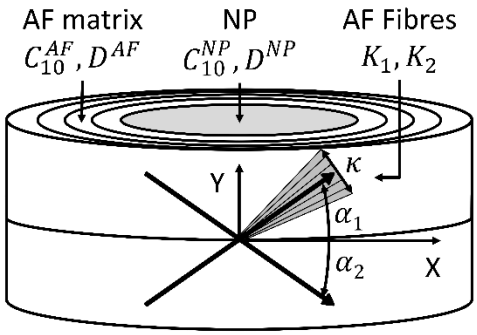

Fig.2. The model features 8 parameters: matrix constants for annulus fibrosus $(\mathrm{C}_{10}^{\mathrm{AF}}, \mathrm{D}^{\mathrm{AF}})$ *and nucleus pulposus* $(\mathrm{C}_{10}^{\mathrm{NP}}, \mathrm{D}^{\mathrm{NP}})$*, fibre stiffness (K1), rate of stiffness increase (K2), average bundle angle* ($\alpha_1 = -\alpha_2 = \alpha$) *and fibre dispersion (κ) around the initial bundle direction.*

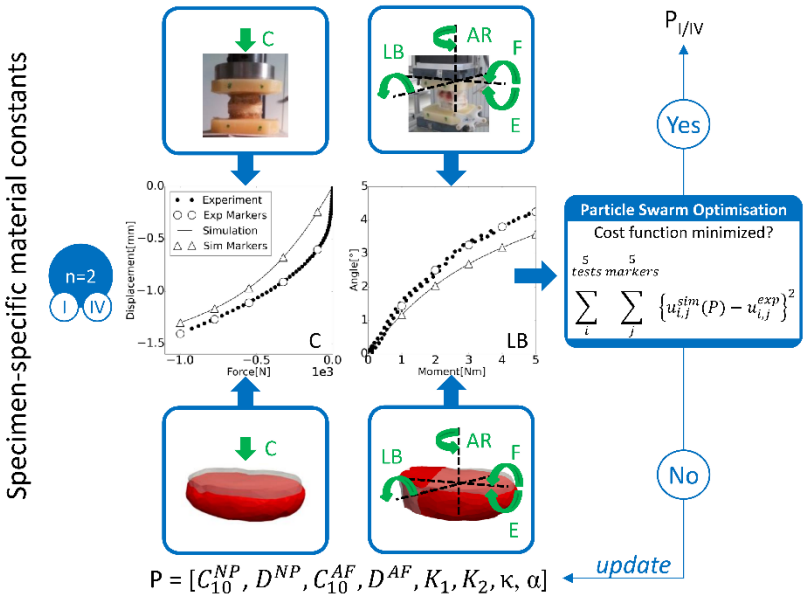

Fig.3. Material parameters for healthy (P_I) and degenerated (P_{IV}) discs were identified against tests. Compression (C), axial torsion (AR), lateral bending (LB), flexion (F) and extension (E) were applied to the IVDs and simulated on their respective MRI-based FE model. Optimisation of P_I and P_{IV} was performed by minimizing differences between experimental (O) and simulated (Δ) markers' deflections u taken at regular load increments.

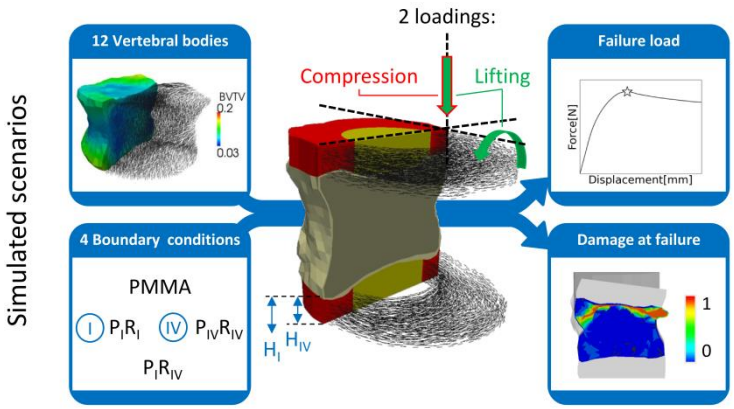

Fig.4. Compression and lifting were applied to 12 vertebral bodies' models. Meshing, bone volume fraction (BVTV) and trabecular anisotropy necessary to compute elastic, plastic and damage behaviour of the bone were determined form the high resolution peripheral QCT data. PMMA embedding, degenerated ($P_{IV}R_{IV}$) and healthy IVDs with healthy thickness (P_IR_I) or degenerated thickness (P_IR_{IV}) were extruded accordingly (H_I or H_{IV}, Eq.6). Finally, load and damage at failure were computed for each boundary condition and loading.

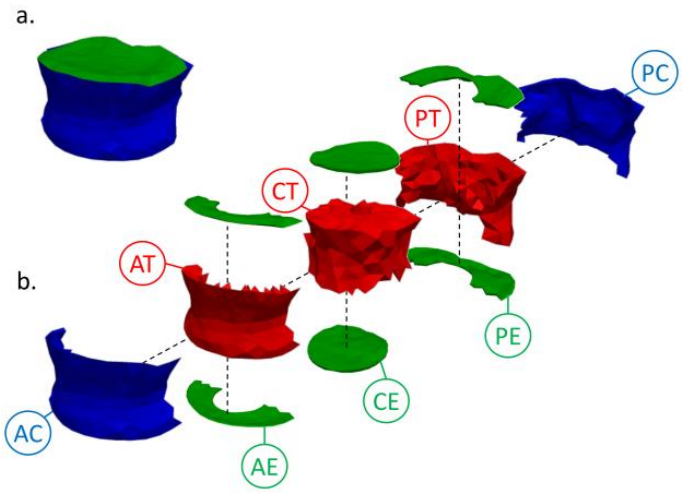

Fig.5. Regions of interest of the vertebral body. Each vertebral body (a.) was divided into 8 regions (b.): anterior and posterior cortical shell (AC / PC), anterior, central and posterior endplates (AE / CE / PE) and trabecular bone (AT / CT / PT). Both endplates are accounted for in AE, CE and PE. AT and PT refer to the trabecular bone elements in contact with the cortical shell (AC and PC). CT represents the trabecular core.

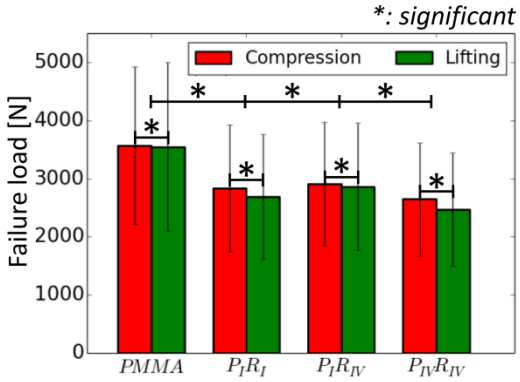

Fig.6. The mean values and standard deviations of the vertebral bodies' failure loads are displayed. All failure loads were significantly different ($p < 0.05$).

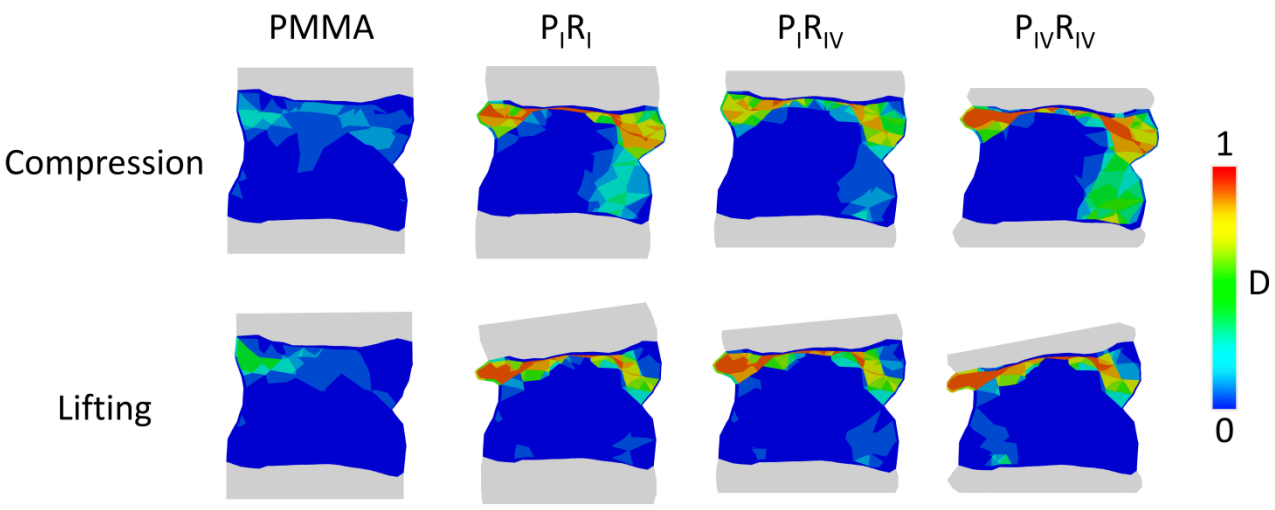

Fig.7. Comparison of the damage patterns within the mid-sagittal section of a typical vertebral body at failure under compression (left) and lifting (right), 0 being the absence of damage and 1 being the complete failure of the element.

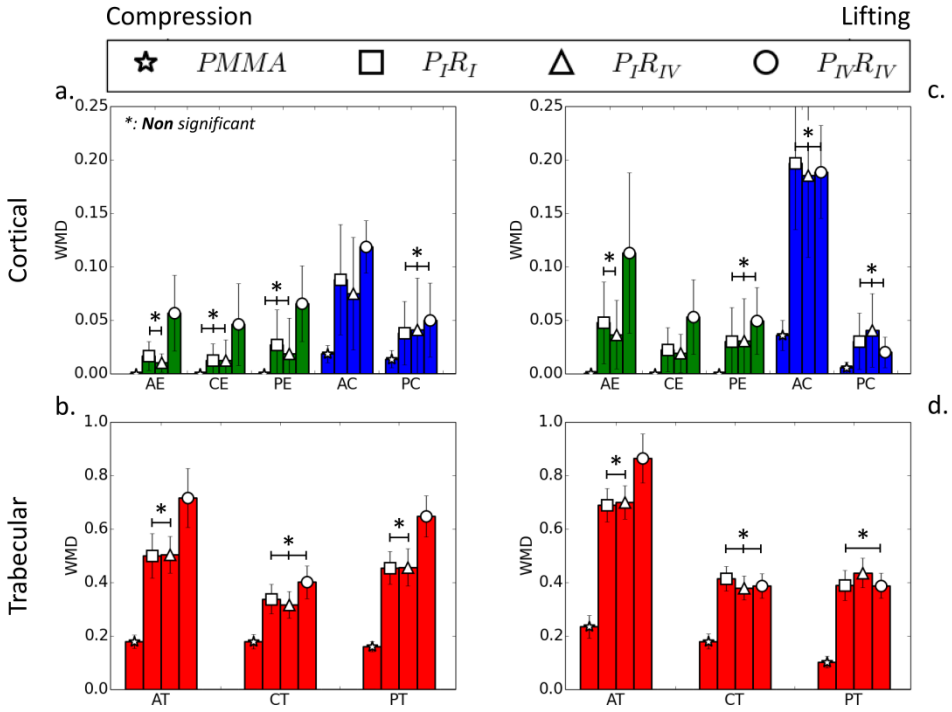

Fig.8. Evaluation of the damage accumulation within the 8 ROIs of the vertebral bodies under compression (a, b) and lifting (c, d). Damage was computed at failure. The WMDs of the cortical components (endplates: AE, CE, PE, cortex: AC, PC) are displayed in (a) and (c). The WMDs of the trabecular bone (AT, CT, PT) are shown in (b) and (d). All WMDs of a ROI were significantly different ($p < 0.05$) unless stated otherwise.

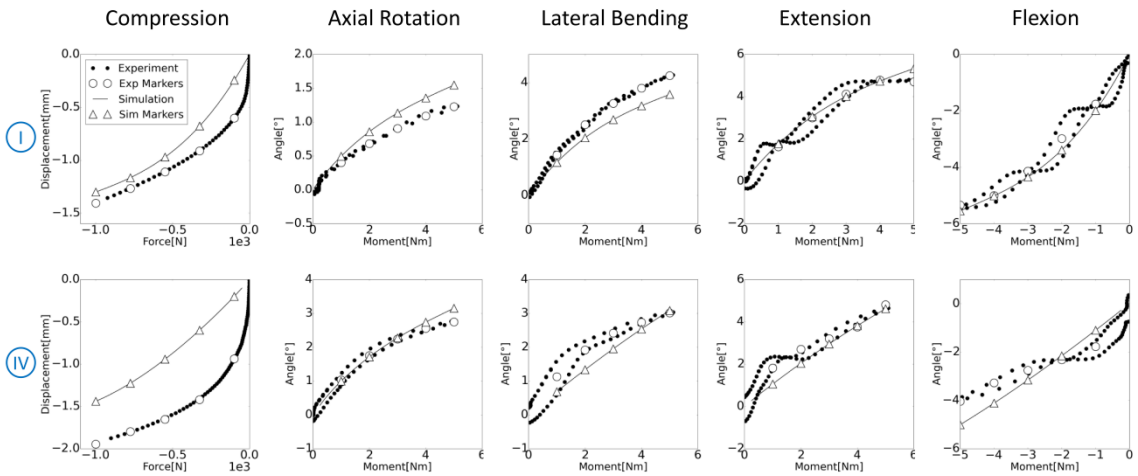

Fig.A1. Experimental and simulated load-deflection curves in compression (C), axial torsion (AR), lateral bending (LB), flexion (F) and extension (E) for both healthy (I) and degenerated (IV) specimens.

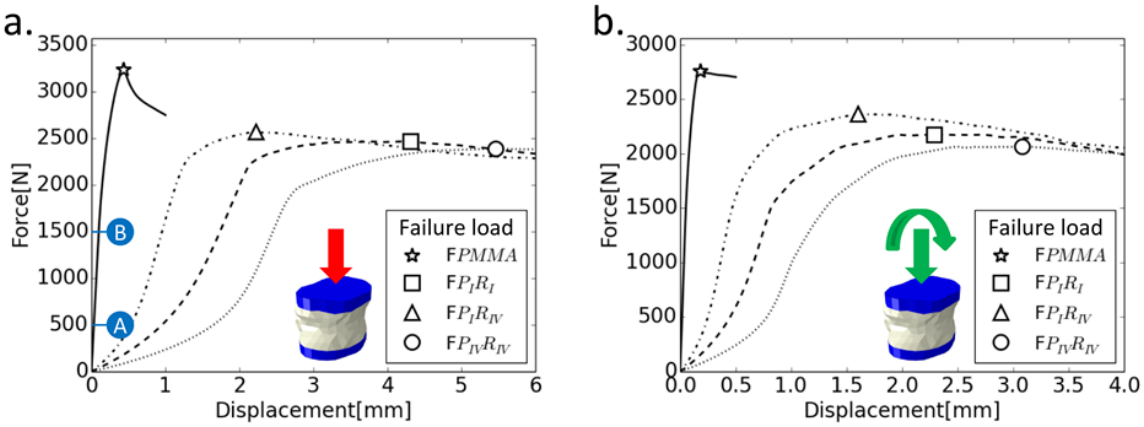

Fig.A2. Force-deflection curves and failure loads computed for the 4 boundary conditions for a typical vertebral body reported for uniaxial compression (a) and lifting (b). For comparison purpose, the maximal force applied on a L1 vertebral body of a 64 years-old man of 60kg while (A) walking slowly (3km/h) and (B) bending to lift 10kg from the floor (Bergmann 2008).

Tables

Table 1. The degeneration scores, height (H), cross-sectional area (CSA) and size ratio (R) were assessed from MRI. Two sets of parameters were identified from the calibration. The calibration quality was assessed via Root Mean Square Error (RMSE) and Concordance Correlation Coefficient (CCC) between simulated and measured load-deflection data (cf. Fig.A1). Experimental ranges of motion (ROM) are also provided.

	Specimen	Ⓘ	Ⓘⓥ
Degeneration	Thompson	1	4
	Watanabe	1	4
	Benneker	0	15
Morphology	H (mm)	9.5	7.8
	CSA (mm^2)	1430	2367
	R	0.25	0.16
Parameters	C_{10}^{NP} (MPa)	0.026	0.173
	D^{NP} (MPa^{-1})	1.31	0.97
	C_{10}^{AF} (MPa)	0.217	0.551
	D^{AF} (MPa^{-1})	1.600	0.481
	K_1 (MPa)	934	42
	K_2	1160	596
	α (°)	35.9	31.7
	κ	0.182	0.270
Exp. ROM	AR (°)	1.2	2.7
	LB (°)	4.2	3.0
	F (°)	-5.3	-4.0
	E (°)	4.7	4.8
	C (mm)	-1.3	-2.0
RMSE	AR (°)	0.23	0.20
	LB (°)	0.53	0.40
	F (°)	0.24	0.44
	E (°)	0.29	0.47
	C (mm)	0.21	0.44
CCC	AR	0.80	0.96
	LB	0.85	0.86
	F	0.98	0.83
	E	0.97	0.92
	C	0.82	0.75
	All 5 tests	0.99	0.99

Table 2. All the failure loads were compared to the compressive strength of the vertebral body with embedded endplates simulated in this study (F_{PMMA}) and measured in vitro in Chevalier et al. 2008 (F_{EXP}). R^2, standard error of the estimate (SEE) and regression equations are provided. All the correlations were highly significant ($p < 0.001$).

	X	Compression					
		F_{PMMA} This study			F_{EXP} Chevalier et al.		
Y		R^2	SEE	Equation	R^2	SEE	Equation
Compression	F_{PMMA}				0.971	0.044	Y=0.673X-31.086
	F_{PIRI}	0.996	0.020	Y=0.800X-12.969	0.978	0.030	Y=0.541X-54.508
	F_{PIRIV}	0.996	0.019	Y=0.782X+118.408	0.979	0.029	Y=0.529X+77.020
	F_{PIVRIV}	0.996	0.016	Y=0.715X+94.632	0.983	0.024	Y=0.485X+51.700
Lifting	F_{PMMA}	0.993	0.03	Y=0.959X-156.507	0.964	0.047	Y=0.645X-185.023
	F_{PIRI}	0.972	0.044	Y=0.688X+9.859	0.963	0.035	Y=0.468X-36.076
	F_{PIRIV}	0.974	0.045	Y=0.726X+64.358	0.971	0.033	Y=0.495X+8.289
	F_{PIVRIV}	0.986	0.030	Y=0.659X+-60.737	0.975	0.027	Y=0.448X-102.850